

Hybrid-type synchronization transitions: where marginal coherence, scale-free avalanches, and bistability live together

Victor Buendía,^{1,2,3} Pablo Villegas,⁴ Raffaella Burioni,^{2,3} and Miguel A. Muñoz¹

¹*Departamento de Electromagnetismo y Física de la Materia e Instituto Carlos I de Física Teórica y Computacional. Universidad de Granada, E-18071 Granada, Spain*

²*Dipartimento di Matematica, Fisica e Informatica, Università di Parma, via G.P. Usberti, 7/A - 43124, Parma, Italy*

³*INFN, Gruppo Collegato di Parma, via G.P. Usberti, 7/A - 43124, Parma, Italy*

⁴*Networks Unit, IMT School for Advanced Studies, Lucca, Italy & Instituto Carlos I de Física Teórica y Computacional. Universidad de Granada, E-18071 Granada, Spain*
(Dated: May 23, 2022)

The human cortex is never at rest but in a state of sparse and noisy neural activity. It has been conjectured that such a state is best described as a critical dynamical process —whose nature is still not fully understood— where scale-free avalanches of activity emerge at the edge of a synchronization phase transition. Using a simple model of coupled excitable oscillators, we rule out standard phase transitions to explain the emergence of collective oscillations, as they do not suffice to explain current experimental evidence. Conversely, we uncover a novel hybrid-type of synchronization transition displaying a very-rich dynamical repertoire supporting all key empirical observations, including scale-free avalanches, marginal coherence, and bistability.

Neurons in the cerebral cortex fire in a rather irregular and sparse way, even in the absence of external stimuli or tasks [1–3]. Understanding the origin and functionality of such an energetically-costly “ground state” is a fundamental question in neuroscience, essential to shed light on how the cortex processes information [4–8].

Two twin sides of spontaneous neuronal activity are *synchronization* and *avalanches*. Depending mostly on cortical regions and functional state, diverse levels of synchronization across a continuum spectrum are observed. Both synchronous and asynchronous states are retained to be important for diverse aspects of information processing; e.g., neuronal synchronization is at the root of collective oscillatory rhythms, a crucial aspect for information transmission between distant areas [9–11] while asynchronous states also play key roles for information coding [12]. Accumulating evidence—including results from the Human Brain Project [13]— suggests that the ground state of spontaneous activity of a healthy cortex lies close to the edge of a synchronization phase transition, neither exceedingly synchronous nor overly incoherent, allowing for transient and flexible levels of coherence, as well as a very-rich dynamical repertoire [8, 13, 14]. Indeed, abnormalities in the synchronization level are linked to pathologies such as Parkinsonian disease (excess) and autism (deficit) [15].

On the other hand, neuronal activity is also observed to propagate in the form of irregular outbursts, termed *neuronal avalanches* [16–18]. These are cascades of activations clustered in time and interspersed by periods of relative quiescence, which have been robustly observed across cortical areas, species, and resolution scales [8, 19, 20]. Avalanche sizes S and durations T are empirically observed to be scale-free, i.e., their associated probability distributions exhibit power-law tails

$P(S) \sim S^{-\tau}$, $P(T) \sim T^{-\alpha}$, and the mean avalanche size obeys $\langle S(T) \rangle \sim T^\gamma$ with γ fulfilling the scaling relation $\gamma = (\alpha - 1)/(\tau - 1)$, a fingerprint of criticality [21, 22].

These empirical observations triggered the development of the “*criticality hypothesis*”, conjecturing that the cortex might extract crucial functional advantages—e.g., large sensitivity and optimal computational capabilities—by operating close to the critical point [16, 19, 20, 23–26]. However, there is still no consensus on what type of phase transition is required for such a critical behavior and diverse explanations for the empirically observed scaling have been put forward [21, 27–30]. Among these, a Landau-Ginzburg (LG) theory was proposed to describe cortical dynamics at a mesoscopic level suggesting that the cortex might operate in a regime close to the edge of a synchronization phase transition at which scale-free avalanches and marginal synchronization occur in concomitance [31], a conclusion that seems to be supported by empirical evidence [13, 32–34] (see also [29, 31, 35–39]). In spite of these advances, a minimal model—simpler than the analytically un-tractable LG theory—capturing the gist of such a rich phenomenology and allowing for in-depth theoretical understanding is still missing.

Here we pose the following questions: do scale-free avalanches possibly occur at the synchronization phase transition of the canonical model for phase synchronization? If not, which is the minimal model for synchronization able to accommodate scale-free avalanches? What type of phase transition does it exhibit? What is its universality class? Answering these questions will pave the road for the more ambitious goal of constructing a statistical mechanics of cortical networks, shedding light onto the collective states that they sustain, as well as advancing our general understanding of phase transitions.

We start by analyzing the canonical model for phase synchronization, customarily used in neuroscience [40–43] and other fields [44]: the Kuramoto model [44–47]. More specifically, given that stochasticity is inherent to neural dynamics and that heterogeneity is not an essential ingredient to generate avalanches [31], we consider a noisy (annealed) version of the model with homogeneous frequencies [43, 44], i.e.

$$\dot{\varphi}_j(t) = \omega + \frac{J}{N} \sum_{i=0}^N \sin(\varphi_i(t) - \varphi_j(t)) + \sigma \eta_j(t) \quad (1)$$

where the phase $\varphi_j(t)$ describes the dynamical state of the j -th oscillatory unit, with $j \in [1, N]$, ω is the common intrinsic frequency, $\eta_j(t)$ a zero-mean unit-variance Gaussian white noise with amplitude σ , and J is the coupling strength with all the neighbors on, e.g., a fully-connected network [44–48]. Eq.(1) exhibits a synchronization phase transition where the synchronization (Kuramoto) order parameter, $Z = \langle e^{i\varphi} \rangle$, experiences a (supercritical) Hopf bifurcation from a fixed point to a limit cycle, revealing the emergence of collective oscillations [47].

Here and in what follows, avalanches are measured following the standard protocol in neuroscience [16, 19], which relies on the identification of individual-unit “spikes” (in this case, crossings over a given phase value) as well as on the definition of a time discretization, needed to cluster close-in-time spikes together [16] (see SI-1). Extensive computational simulations (reported in detail in SI-2) reveal that neither at the critical point nor around it scale-free avalanches exist; $P(S)$ and $P(T)$ always show exponential decays. The ultimate reason for this could be that, at a Hopf bifurcation, oscillations emerge with a fixed non-vanishing frequency [49], setting a characteristic time scale, at odds with scale invariance.

In order to search for a better suited minimal model, we scrutinize the Landau-Ginzburg theory in [31]. In a nutshell, the LG model consists of a set of diffusively coupled units, each of which represents a mesoscopic region of the cortex, and is described by a set of two dynamical equations for the local density of: (i) neuronal activity and (ii) available synaptic resources, respectively (see SI-3 for details). A salient feature is that, as the control parameter (maximum amount of synaptic resources) is increased, individual units experience an *infinite-period bifurcation* from a low-activity fixed point to a limit cycle—with zero-frequency and fixed-amplitude at the bifurcation point—where both activity and synaptic resources oscillate in a “spike-like” manner (i.e., with a phase-dependent velocity). Moreover, single units can produce spikes even when they are slightly below the bifurcation point owing to the effect of noise, in other words, they behave as *type-I excitable units* [50, 51] (see SI-4 for a brief account of excitability types). Finally, by further increasing the control parameter, the coupled oscillatory units become synchronized and, at the

edge of such a synchronization phase transition, scale-free avalanches emerge [31].

Guided by these observations, we consider a set of coupled oscillatory units, each of them represented by the canonical form of type-I excitable units or “active rotors” as defined by $\dot{\varphi} = \omega + a \sin \varphi$, where ω and a are parameters [49, 53]. For $a > \omega$ the deterministic dynamics of each isolated unit exhibits a stable fixed point at $\varphi^* = -\arcsin(\omega/a)$, as well as a saddle with the opposite sign. If a stochastic term $\sigma \eta(t)$ is added, it can induce fluctuations beyond the saddle, thus generating large excursions of the phase before relaxing back to its equilibrium (i.e., the system is type-I excitable, SI-4). Instead, for $a < \omega$ the system just oscillates with phase-dependent angular velocity, and as the “saddle-node into invariant circle” (SNIC) bifurcation point $a_c = \omega$ is approached, the frequency of the oscillations vanishes, implying that the period becomes infinite, while the amplitude remains constant, in full analogy with the LG model. Thus, the full model reads

$$\dot{\varphi}_j = \omega + a \sin \varphi_j + \frac{J}{M_j} \sum_{i \in n.n.j}^{M_j} \sin(\varphi_i - \varphi_j) + \sigma \eta_j(t), \quad (2)$$

where the sum runs over the (M_j) nearest neighbors of unit $j \in 1, 2, \dots, N$ in a given network. We consider versions of the model embedded on fully-connected (FC) networks ($M_j = N, \forall j$), which are useful for analytical approaches and—in analogy with the LG theory—on two-dimensional (2D) lattices (as, at large scales, the cortex can be treated as a 2D sheet [8]). Eq.(2) is sometimes called Shinomoto-Kuramoto model or Winfree’s ring model [52, 54] and has been analyzed in diverse contexts [52, 55–57]. Its collective state can be quantified by the Kuramoto-Daido parameters: $Z_k = \langle e^{ik\varphi} \rangle \equiv \frac{1}{N} \sum_{j=1}^N e^{ik\varphi_j} \equiv R_k e^{i\psi_k}$ (with $k = 1, 2, \dots, \infty$), which, for $k = 1$, is the usual Kuramoto parameter. Analytical progress is achieved in a mean-field approximation (exact for infinitely large FC networks) by (i) writing down a continuity (Fokker-Planck) equation for the probability distribution of phase values, $P(\varphi, t)$ [47, 52, 55–57], (ii) expanding $P(\varphi, t)$ in power series, and (iii) writing an infinite hierarchy of coupled equations for its coefficients (which coincide with the Z_k ’s; see SI-5 and [52, 56]):

$$\begin{aligned} \dot{Z}_k = & Z_k \left(i\omega k - \frac{k^2 \sigma^2}{2} \right) + \frac{ak}{2} (Z_{k+1} - Z_{k-1}) \\ & + \frac{Jk}{2} (Z_1 Z_{k-1} - \bar{Z}_1 Z_{k+1}). \end{aligned} \quad (3)$$

where the bar stands for complex conjugate. The associated phase diagram has been scrutinized in the literature by using different low-dimensional closures for this infinite hierarchy of coupled equations. For instance, using the Ott-Antonsen (OA) ansatz [58] or other more-refined closures [56, 57], one can obtain the phase diagram, summarized in Fig.1 (details in SI-6 and SI-7). It

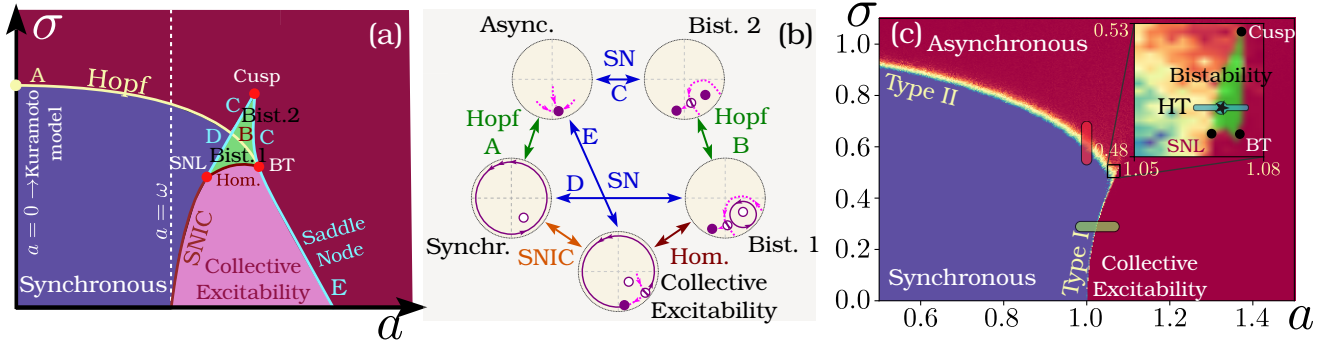


FIG. 1. **Phase diagram and bifurcations of Eq.(2) on a fully-connected network.** (a) Sketch of the phase diagram obtained solving Eqs.(3) using different ansatz; it reveals the existence of synchronous (oscillatory) and asynchronous (non-oscillatory) states, as well as a collectively-excitable regime, separated by diverse types of bifurcations for the collective order parameter. The central triangular-shaped region (green) describes a regime of bistability; its vertices correspond to codimension-2 bifurcations: a saddle-node loop (SNL), a Bogdanov-Takens (BT) and a cusp. Finally, there is also a homoclinic line (Hom) linking the SNL and the BT points. (b) Sketch of the different regimes represented in terms of the complex Kuramoto order parameter. Each regime is represented by a point in the unit circle (since $|Z| \leq 1$) with filled circles describing stable fixed points, open circles standing for unstable fixed points, and mixed-color circles describing saddles. Bifurcations between different regimes are indicated as arrows, labeled with capital characters as in panel (a). (c) Phase diagram computed using direct simulations of a fully-connected network with $N = 5000$ oscillators ($\omega = 1$, $J = 1$). Collective oscillations are computationally detected with the Shinomoto-Kuramoto order parameter (see SI-7) [52]. The location of the bistability region was established by numerically solving Eq.(3) for the first $k = 50$ harmonics ($Z_{51} = 0$). The inset shows a zoom of the bistability region, where codimension-2 points are marked; a star indicates a point with scale-free avalanches. The three segments (red, green and blue) indicate three possible types of transition to synchronization (as considered in Fig.2 and 3)

reveals that there are two main types of collective dynamical regimes: oscillations (synchronous states) and stable fixed points (corresponding to either high-activity asynchronous states in the upper part of the diagram or low activity states in the lower/right part). These are separated by different types of bifurcation lines. In particular, for low noise amplitudes, σ , as the control parameter a is increased there is a collective SNIC bifurcation from the collective oscillatory regime to a stable fixed point characterized by very-low spiking activity, but susceptible to collectively-react to external inputs, called *collective-excitability* phase; in analogy with the classification of excitability types we refer to this as *type-I synchronization transition*. Conversely, for small values of a , by increasing σ one encounters a collective Hopf bifurcation, a *type-II synchronization transition*, to a high-activity asynchronous state (see SI-4 for further details on neuronal excitability classes and synchronization types). Remarkably, these two bifurcation lines cannot possibly intersect each other owing to topological reasons [50], so there is not such a thing as a “tricritical” point. Instead, in the region where the above two bifurcation lines come close to each other, there exists a region of bistability (green area in Fig.1a) [55, 59] delimited by three co-dimension-2 bifurcations: (marked with red circles in Fig.1b): a *Bogdanov-Takens* (BT) point, where the Hopf-bifurcation line finishes, colliding tangentially with a line of saddle-node bifurcations; a *saddle-node-loop* (SNL) where the line of SNIC bifurcations ends, becoming a standard saddle-node line; and a *cusp*, where

two saddle-node bifurcation lines collide. Observe that the bistability region is divided into two halves by the line of Hopf bifurcations, so the regime of collective excitability coexists with either oscillations below the Hopf line or the high-activity asynchronous state above the Hopf line. In other words, in this region the Hopf bifurcation occurs in one of the branches of two coexisting solutions, i.e., in concomitance with bistability.

In order to obtain a highly-accurate phase diagram, needed for forthcoming analyses, we complemented the above analytical approximations with extensive computational analyses of the full stochastic system (size $N = 10^4$) as well as a direct numerical-integration of Eq.(3) truncated at sufficiently large values of k ($k = 50$). Results of this combined approach are summarized in Fig.1c which shows that the overall shape of the phase diagram is qualitatively identical to the one predicted by low-dimensional closures, but the bistability region is reduced to a small region (inset of Fig.1c). Importantly, a very-similar phase diagram is found when the model is simulated onto a 2D lattice (including also a bistability region and richer spatio-temporal patterns, see SI-8).

The moral of these findings is that, in order to analyze generic transitions from asynchronous to synchronous phases, one should consider not only the standard type-I and type-II cases, but also more complex scenarios. In particular, there is an intermediate situation where the transition to synchrony occurs in concomitance with bistability, i.e., when incipient oscillations coexist with low-activity asynchronous states, that we call “*hybrid-*

type (HT) synchronization transition”.

Fig.2 shows representative raster plots around the three different types of transition under scrutiny (colored segments in Fig.1c identify these three examples in the phase diagram): type-I (SNIC), type-II (Hopf), and HT synchronization transition, respectively, showing results slightly within the synchronous phase (left), very close to criticality (central), and in the asynchronous phase (right). Naked-eye inspection reveals that raster plots nearby the HT transition reflect a much richer structure (see below). Following the protocol for avalanche detec-

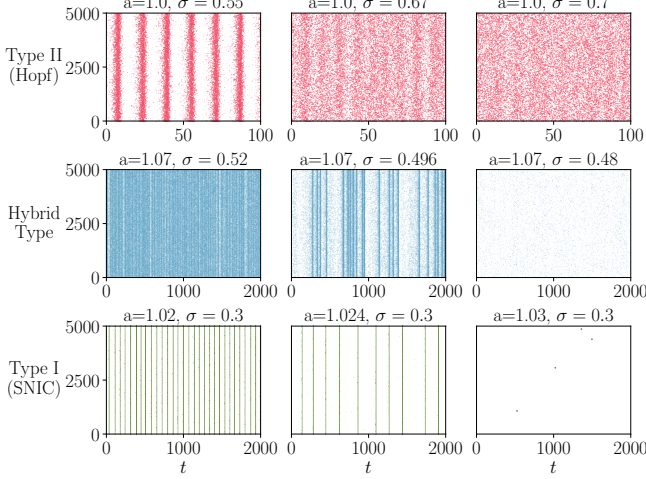


FIG. 2. Raster plots in a fully-connected network of size $N = 5000$ for each of the three considered cases (as indicated in Fig.1c) — Hopf (type-II) bifurcation, hybrid-type (HT) synchronization, and SNIC(type-I) bifurcation (from top to bottom)— in the synchronous phase (left column), right at the transition point or very slightly within the synchronous/oscillatory phase (central column), and in the asynchronous phase (right column).

tion (SI-1) we determined the statistics of avalanche sizes and durations in these three scenarios.

As shown in Fig.3 for FC networks, power-law distributed avalanches do not emerge at the type-II (Hopf) transition (red lines in Fig.3) nor at the type-I (green dots in Fig.3) at which there are large collective spiking events recruiting most of the units in the system into huge avalanches, separated by extremely long periods of quiescence (as illustrated in Fig.2). On the contrary, when crossing through the HT transition, clean scale-invariant avalanche distributions are observed at criticality; these span across many decades and obey finite-size scaling (see Fig.3c, Fig.3d as well as SI-7). More specifically, at the HT transition, we obtain exponent values $\tau \approx 2.1(1)$, $\alpha \approx 2.5(1)$ and $\gamma^{-1} \approx 0.75(5)$ [60, 61] (compatible with values in [38]). Analogous results are found for 2D lattices (with $\tau \approx 1.7(1)$, $\alpha \approx 1.9(1)$ and $\gamma^{-1} \approx 0.75(5)$, compatible with the values reported in experimental works [28]). In both cases, the scaling re-

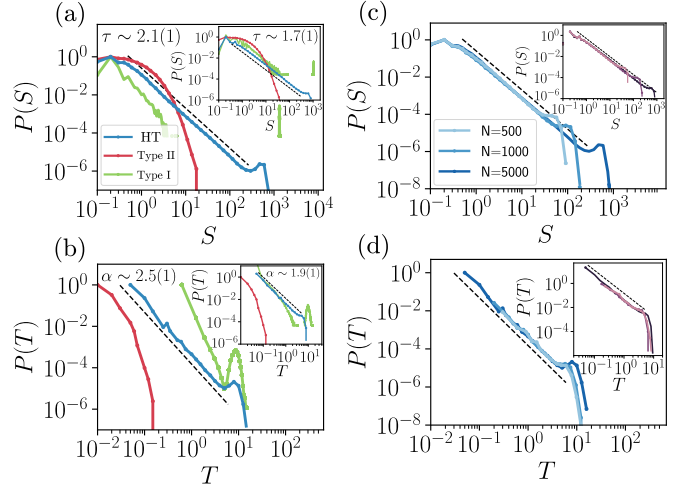


FIG. 3. **Avalanche distributions.** (a,b) Avalanche-size and duration distributions for three different types of synchronization transitions (right at the transition points): type-I (SNIC) transition (green lines, $a = 1.024$, $\sigma = 0.3$); type-II (Hopf) transition (red lines, $a = 1.04$, $\sigma = 0.575$), and HT transition (blue lines, $a = 1.07$, $\sigma = 0.499$) in FC networks ($N = 5000$). Only the last one exhibits clear cut power-law behavior, both for size and duration distributions. **Insets:** As in the main Figure but for simulations in a 2D lattice (size 64^2): type-I transition ($a = 0.99$, $\sigma = 0.05$), type-II transition ($a = 0.60$, $\sigma = 0.64$), and HT synchronization transition ($a = 0.98$, $\sigma = 0.185$). (c,d) Finite-size scaling analysis of $P(S)$ and $P(T)$ in FC networks of different sizes (as specified in the legend) in the HT regime. **Insets:** As in the main Figures but for 2D lattices of sizes ($N = 16^2$, $N = 32^2$, $N = 64^2$).

lation holds and the corresponding values of γ coincide with its seemingly super-universal value reported in [28].

As a complementary measure of complexity at the different types of transition points, we also computed the probability distribution of the inter-spike intervals (ISI), along with its associated coefficient of variation (CV). Only around the HT transition, within the bistability region, we found large coefficients of variation $CV > 1$ and extremely broad distributions of ISI values (see SI-7), revealing the presence of complex time series with a high level of variability, similar to that observed in the cortex. Thus, even if type-I and type-II synchronization transitions are well-known to exhibit signatures of criticality such as finite-size scaling (see e.g. [62] and [63], respectively), unlike to HT transitions, they are not able to generate the higher levels of complexity required for scale-free avalanches and large dynamical repertoires.

One could wonder whether such a rich phenomenology emerging around the HT transitions stems from any of the special codimension-2 bifurcation in the phase diagram. Remarkably, the saddle-node-loop (SNL) bifurcation has been previously argued to be necessary for the generation of high variability and dynamical richness in neural networks [64, 65] and it has also been established

that the crucial features of balanced excitation/inhibition neural networks stem from a phase diagram organized around a BT bifurcation with bistability [66, 67].

As illustrated in the actual phase diagram (see Fig.1 and its 2D counterpart in SI-8) the bistability region is rather small in the parameter space so that all the discussed singular points are extremely close to each other. Thus, providing a clear-cut computational answer to the question above is a very hard problem. Numerically, we can just conclude that scale-free avalanches appear when entering the synchronous phase within the bistability region, most likely at the Hopf bifurcation, but in the close vicinity of such codimension-2 bifurcations.

An aspect that needs further analysis is the relationship between criticality and bistability: these two features are usually opposed to each other, as they correspond to either continuous or discontinuous phase transitions, respectively. However, the onset of synchronization in the HT transition occurs within a region of bistability. The intertwining between criticality and bistability is most likely at the basis of the very rich dynamical repertoires reported for the HT case. It is very plausible, that the above-described Landau-Ginzburg theory, as well as possibly other models [38], exhibit scale-free avalanches at the edge of synchronization, since some kind of bistability is also present around the synchronization transition.

Remarkably, the reported complex triangular-shaped structure is rather universal and emerges in other models exhibiting a both type-I and type-II transitions (see e.g. [50, 68–70]); in particular, it appears in the paradigmatic and broadly used (Wilson-Cowan) model of excitatory-inhibitory networks [71]. Thus, the phenomenology discussed here is rather universal and not model-specific. It is noteworthy that other scenarios have been described to connect lines of type-I and type-II transitions –e.g., subcritical Hopf bifurcations followed by a fold of limit cycles– which also involve a regime of bistability (see [37]). The exciting possibility that scale-free avalanches can also emerge in such cases will be investigated elsewhere.

Even if the minimal model studied here is exceedingly simple to be a realistic model of the cortex, it can provide us with insight on the basic dynamical mechanisms needed to generate its complex dynamical features. Furthermore, it is well-established that diverse control, self-organization mechanisms are able to regulate a network to lie around some target regime or point [72–74]. Thus, a cortical neural network with dynamics akin to that of the present simple model could be self-organized to the region near the HT synchronization transition [74–76], and by doing so, it could rapidly shift its behavior from synchronous to asynchronous, to collective excitability, or to up-and-down transitions in a dynamical way, allowing for an extremely rich and flexible dynamical repertoire derived from operating at such an “edge of the edge”.

We hope this work opens the door for new theoretical investigations (including renormalization group analyses [77]) of some of the remaining puzzling and unsolved issues, paving the way to the long term to the goal of constructing a statistical-mechanics of the cortex.

MAM acknowledges the Spanish Ministry and Agencia Estatal de investigación (AEI) through grant FIS2017-84256-P (European Regional Development Fund), as well as the Consejería de Conocimiento, Investigación Universidad, Junta de Andalucía and European Regional Development Fund, Ref. A-FQM-175-UGR18 and SOMM17/6105/UGR for financial support. V.B and R.B. acknowledge funding from the INFN BIOPHYS project. We also thank Cariparma for their support through the TEACH IN PARMA project. We thank S. di Santo and G. Barrios for very valuable discussions.

-
- [1] W. R. Softky and C. Koch, *J. Neurosci.* **13**, 334 (1993).
 - [2] A. Arieli, A. Sterkin, A. Grinvald, and A. Aertsen, *Science* **273**, 1868 (1996).
 - [3] M. Abeles, *Corticonics: Neural circuits of the cerebral cortex* (Cambridge University Press, Cambridge, 1991).
 - [4] P. E. Latham, B. J. Richmond, P. G. Nelson, and S. Nirenberg, *J. Neurophysiol.* **83**, 808 (2000).
 - [5] M. Mattia and M. V. Sanchez-Vives, *Cogn. Neurodynamics* **6**, 239 (2012).
 - [6] Y. Ahmadian and K. D. Miller, *arXiv preprint arXiv:1908.10101* (2019).
 - [7] G. Deco, V. K. Jirsa, P. A. Robinson, M. Breakspear, and K. Friston, *PLoS Comput. Biol.* **4** (2008).
 - [8] M. Breakspear, *Nat. Neurosci.* **20**, 340 (2017).
 - [9] G. Buzsaki, *Rhythms of the Brain* (Oxford Univ. Press, Oxford, 2009).
 - [10] L. Muller, F. Chavane, J. Reynolds, and T. J. Sejnowski, *Nat. Rev. Neurosci.* **19**, 255 (2018).
 - [11] A. Buehlmann and G. Deco, *PLoS Comput. Biol.* **6** (2010).
 - [12] A. Renart, J. De La Rocha, P. Bartho, L. Hollender, N. Parga, A. Reyes, and K. D. Harris, *science* **327**, 587 (2010).
 - [13] H. Markram, E. Muller, S. Ramaswamy, M. W. Reimann, M. Abdellah, C. A. Sanchez, A. Ailamaki, L. Alonso-Nanclares, N. Antille, S. Arsever, *et al.*, *Cell* **163**, 456 (2015).
 - [14] J. Cabral, M. L. Kringelbach, and G. Deco, *NeuroImage* **160**, 84 (2017).
 - [15] E. R. Kandel, J. H. Schwartz, T. M. Jessell, S. A. Siegelbaum, and A. J. Hudspeth, *Principles of Neural Science*, Vol. 4 (McGraw-hill, New York, 2000).
 - [16] J. M. Beggs and D. Plenz, *J. Neurosci.* **23**, 11167 (2003).
 - [17] T. Petermann, T. C. Thiagarajan, M. A. Lebedev, M. A. Nicolelis, D. R. Chialvo, and D. Plenz, *Proc. Natl. Acad. Sci. USA* **106**, 15921 (2009).
 - [18] T. Bellay, A. Klaus, S. Seshadri, and D. Plenz, *Elife* **4**, e07224 (2015).

- [19] D. Plenz and E. Niebur, *Criticality in Neural Systems* (John Wiley & Sons, New York, 2014).
- [20] D. R. Chialvo, Nat. Phys. **6**, 744 (2010).
- [21] N. Friedman, S. Ito, B. A. W. Brinkman, M. Shimono, R. E. L. DeVille, K. A. Dahmen, J. M. Beggs, and T. C. Butler, Phys. Rev. Lett. **108**, 208102 (2012).
- [22] M. A. Muñoz, R. Dickman, A. Vespignani, and S. Zapperi, Phys. Rev. E **59**, 6175 (1999).
- [23] T. Mora and W. Bialek, J. Stat. Phys. **144**, 268 (2011).
- [24] M. A. Muñoz, Rev. Mod. Phys. **90**, 031001 (2018).
- [25] J. Zierenberg, J. Wilting, and V. Priesemann, Phys. Rev. X **8**, 031018 (2018).
- [26] J. Wilting, J. Dehning, J. Pinheiro Neto, L. Rudelt, M. Wibral, J. Zierenberg, and V. Priesemann, Front. Syst. Neurosci. **12**, 55 (2018).
- [27] A. Ponce-Alvarez, A. Jouary, M. Privat, G. Deco, and G. Sumbre, Neuron **100**, 1446 (2018).
- [28] A. J. Fontenele, N. A. de Vasconcelos, T. Feliciano, L. A. Aguiar, C. Soares-Cunha, B. Coimbra, L. Dalla Porta, S. Ribeiro, A. J. Rodrigues, N. Sousa, P. V. Carelli, and M. Copelli, Phys. Rev. Lett. **122**, 208101 (2019).
- [29] L. Dalla Porta and M. Copelli, PLoS Comput. Biol. **15**, e1006924 (2019).
- [30] M. Yaghoubi, T. de Graaf, J. G. Orlandi, F. Giroto, M. A. Colicos, and J. Davidsen, Sci. Rep. **8**, 3417 (2018).
- [31] S. di Santo, P. Villegas, R. Burioni, and M. A. Muñoz, Proc. Natl. Acad. of Sci. U.S.A. **115**, E1356 (2018).
- [32] E. D. Gireesh and D. Plenz, Proc. Natl. Acad. Sci. USA **105**, 7576 (2008).
- [33] H. Yang, W. L. Shew, R. Roy, and D. Plenz, J. Neurosci. **32**, 1061 (2012).
- [34] S. R. Miller, S. Yu, and D. Plenz, Sci. Rep. **9**, 1 (2019).
- [35] S.-S. Poil, R. Hardstone, H. D. Mansvelder, and K. Linkenkaer-Hansen, J. Neurosci. **32**, 9817 (2012).
- [36] D.-P. Yang, H.-J. Zhou, and C. Zhou, PLoS Comput. Biol. **13**, e1005384 (2017).
- [37] I. I. Lima Dias Pinto and M. Copelli, Phys. Rev. E **100**, 062416 (2019).
- [38] J. Liang, T. Zhou, and C. Zhou, arXiv preprint arXiv:2001.05626 (2020).
- [39] F. Pittorino, M. Ibáñez Berganza, M. di Volo, A. Vezzani, and R. Burioni, Phys. Rev. Lett. **118**, 098102 (2017).
- [40] M. Breakspear, S. Heitmann, and A. Daffertshofer, Front. Human Neurosci. **4**, 190 (2010).
- [41] J. Cabral, E. Hugues, O. Sporns, and G. Deco, Neuroimage **57**, 130 (2011).
- [42] F. A. Ferrari, R. L. Viana, S. R. Lopes, and R. Stoop, Neural Networks **66**, 107 (2015).
- [43] P. Villegas, P. Moretti, and M. A. Muñoz, Sci. Rep. **4**, 5990 (2014).
- [44] A. Pikovsky, M. Rosenblum, and J. Kurths, *Synchronization: A Universal Concept in Nonlinear Sciences*, Vol. 12 (Cambridge university press, Cambridge, 2003).
- [45] Y. Kuramoto, Lecture Notes in Physics **39**, 420 (1975).
- [46] Y. Kuramoto, *Chemical oscillations, waves, and turbulence* (Courier Corporation, New York, 2003).
- [47] J. A. Acebrón, L. L. Bonilla, C. J. Pérez Vicente, F. Ritort, and R. Spigler, Rev. Mod. Phys. **77**, 137 (2005).
- [48] S. H. Strogatz, Physica D **143**, 1 (2000).
- [49] S. H. Strogatz, *Nonlinear Dynamics and Chaos: With Applications to Physics, Biology, Chemistry, and Engineering*, Studies in Nonlinearity (Addison-Wesley Pub, Reading, Mass, 1994).
- [50] E. M. Izhikevich, *Dynamical Systems in Neuroscience: The Geometry of Excitability and Bursting* (The MIT Press, Cambridge, 2006).
- [51] B. Lindner, J. García-Ojalvo, A. Neiman, and L. Schimansky-Geier, Phys. Rep. **392**, 321 (2004).
- [52] S. Shinomoto and Y. Kuramoto, Prog. Theor. Phys. **75**, 1105 (1986).
- [53] R. Adler, Proc. IEEE **34**, 351 (1946).
- [54] A. T. Winfree, *The Geometry of Biological Time*, Vol. 12 (Springer, Berlin, 2001).
- [55] H. Sakaguchi, S. Shinomoto, and Y. Kuramoto, Prog. Theor. Phys. **77**, 1005 (1987).
- [56] M. A. Zaks, A. B. Neiman, S. Feistel, and L. Schimansky-Geier, Phys. Rev. E **68** (2003).
- [57] I. V. Tyulkina, D. S. Goldobin, L. S. Klimenko, and A. Pikovsky, Phys. Rev. Lett. **120** (2018).
- [58] E. Ott and T. M. Antonsen, Chaos **19**, 023117 (2009).
- [59] L. M. Childs and S. H. Strogatz, Chaos **18**, 043128 (2008).
- [60] J. Alstott, E. Bullmore, and D. Plenz, PLoS one **9** (2014).
- [61] A. Clauset, C. R. Shalizi, and M. E. Newman, SIAM review **51**, 661 (2009).
- [62] H. Ohta and S. I. Sasa, Phys. Rev. E **78**, 065101 (2008).
- [63] H. Hong, H. Chaté, L.-H. Tang, and H. Park, Phys. Rev. E **92** (2015).
- [64] J. Hesse, J.-H. Schleimer, and S. Schreiber, Phys. Rev. E **95** (2017).
- [65] J.-H. Schleimer, J. Hesse, and S. Schreiber, arXiv:1902.00951 (2019), arXiv:1902.00951 [q-bio].
- [66] J. D. Cowan, J. Neuman, and W. van Drongelen, J. Math. Neurosci. **6**, 1 (2016).
- [67] M. Benayoun, J. D. Cowan, W. van Drongelen, and E. Wallace, PLoS Comput. Biol. **6**, e1000846 (2010).
- [68] K. Tsumoto, H. Kitajima, T. Yoshinaga, K. Aihara, and H. Kawakami, Neurocomputing **69**, 293 (2006).
- [69] C. R. Laing, J. Math. Neurosci. **8**, 4 (2018).
- [70] E. Montbrió, D. Pazó, and A. Roxin, Phys. Rev. X **5** (2015).
- [71] R. M. Borisjuk and A. B. Kirillov, Biol. Cybern. **66**, 319.
- [72] J. Bonachela, S. de Franciscis, J. Torres, and M. A. Muñoz, J. Stat. Mech.: Theory Exp. **2010**, P02015 (2010).
- [73] M. Girardi-Schappo, L. Brochini, A. A. Costa, T. T. A. Carvalho, and O. Kinouchi, Phys. Rev. Res. **2**, 012042 (2020).
- [74] V. Buendía, S. di Santo, J. A. Bonachela, and M. A. Muñoz, arXiv preprint arXiv:2006.03020 (2020).
- [75] S. di Santo, R. Burioni, A. Vezzani, and M. A. Muñoz, Phys. Rev. Lett. **116**, 240601 (2016).
- [76] V. Buendía, S. di Santo, P. Villegas, R. Burioni, and M. A. Muñoz, Phys. Rev. Res. **2**, 013318 (2020).
- [77] L. Meshulam, J. L. Gauthier, C. D. Brody, D. W. Tank, and W. Bialek, Physical review letters **123**, 178103 (2019).

Supplementary Information: Hybrid-type synchronization transitions: where marginal coherence, scale-free avalanches, and bistability live together

Victor Buendía,^{1,2,3} Pablo Villegas,⁴ Raffaella Burioni,^{2,3} and Miguel A. Muñoz¹

¹*Departamento de Electromagnetismo y Física de la Materia e Instituto Carlos I de Física Teórica y Computacional. Universidad de Granada, E-18071 Granada, Spain*

²*Dipartimento di Matematica, Fisica e Informatica,
Università di Parma, via G.P. Usberti, 7/A - 43124, Parma, Italy*

³*INFN, Gruppo Collegato di Parma, via G.P. Usberti, 7/A - 43124, Parma, Italy*

⁴*Networks Unit, IMT School for Advanced Studies, Lucca,
Italy & Instituto Carlos I de Física Teórica y Computacional. Universidad de Granada, E-18071 Granada, Spain*

CONTENTS

1. Definition and measurement of avalanches	2
2. Avalanches in the stochastic Kuramoto model	2
3. Bifurcations in the single unit of the Landau-Ginzburg model	4
4. A note on different types of excitability and bifurcations	5
5. Mathematical analysis of globally coupled oscillators	6
5.1. Order-parameter equations	6
5.2. Approximate solutions or closures	7
6. Bifurcation analysis of the Ott-Antonsen equations	8
7. Computational analyses and results	10
7.1. Phase diagram of the full model	10
7.2. Accuracy of different closures	11
7.3. Avalanches at different types of bifurcations	11
7.4. Dynamical variability	13
8. Phase diagram for the model on two-dimensional lattices	14
References	16

1. DEFINITION AND MEASUREMENT OF AVALANCHES

The protocol to measure neuronal avalanches is based on the one first proposed by Beggs and Plenz [1], that has been widely employed in the analysis of both experimental and theoretical data (e.g. [2–6]). This protocol allows one to study in detail the structure of the spatiotemporal clusters of neuronal “activity”, e.g. spikes in individual neurons or peaks of the negative local field potentials. Here, we discuss specifically how the protocol is adapted for the case considered in this paper of phase oscillators.

1. For each individual unit j , one needs to define its “activity”. A “spike” of activity of a given oscillator j is a transient event occurring whenever its phase $\varphi_j(t)$ crosses a given threshold value. In particular, it is possible to define $y_j = 1 + \sin \varphi_j$ that takes large (resp. small) values (close to 2, resp 0) when the phase crosses $\pi/2$ (resp. $-\pi/2$).
2. A threshold y_{th} is defined such that whenever y_j crossed, a “spiking event” starts to be tracked; it finishes when y_j goes again below threshold. The total integral of $y_j - y_{\text{th}}$ along such a large-activity time window is the size s_j of the local event at the initiation time t_j^k . $k = 1, 2, \dots$, etc. label the sequence of spikes.
3. The full set of spikes for all units j (at times t_j^k and sizes s_j^k) defines a raster plot employed for the subsequent analyses.
4. The inter-spike interval (ISI) between all couples of consecutive spikes (regardless of which unit generated them) is computed, and its probability distribution $P(\text{ISI})$ and its average value $\langle \text{ISI} \rangle$ are computed. A time scale $\Delta t = \langle \text{ISI} \rangle$ is used to discretize the raster plots in time bins.
5. An avalanche is defined as a series of spikes in between two empty bins (with no spike) such that all consecutive time bins include some activity. The sum of all s_j^k in between such two empty bins is the avalanche size S , while avalanche duration T is defined as the time elapsed between the two limiting empty bins.
6. The probability distribution function (histogram) of avalanche sizes and durations is then computed.

The empirical detection of avalanches in noisy data and/or in continuous time series is often exposed to some potential pitfalls that is important to underline.

- First of all, it relies on an arbitrary choice of a threshold for the detection of “spikes” of activity. In our case, selecting a threshold y_{th} (e.g. $y_{\text{th}} = 1.6$) ensures that background noise around the fixed point is filtered and only significant excursions in the phase value are considered.
- It also relies on the choice of the time bin size as the average inter-spike interval; this choice has been made in accordance with the usual one in neuroscience analyses [1, 2, 4, 7].
- Let us also remark that, instead of using the activity y_j with its corresponding threshold, we could have defined a “spike” each time oscillator hits a predefined phase value, such as $\pi/2$. In our particular case, the choice of definition of activity as the sine of the phase is influenced by [5]. We integrate over an interval to compute s_j given that each oscillator represents a mesoscopic cortical region in which activity is not point-like (as, it can be, for example, in individual neurons when represented as oscillators; see e.g. [8]).
- Let us finally stress that computational model analyses, as the ones reported here, do not suffer from *severe* subsampling effects that may strongly impair empirical measurements of avalanches [9–11]

2. AVALANCHES IN THE STOCHASTIC KURAMOTO MODEL

Without loss of generality, we fix $J = 1$ and $\omega = 1$ [12], leaving σ as the only free parameter. Then, $\sigma_c = 1$ indicates the critical point for infinitely large systems. Due to the finite size N of the considered networks, the precise location of the critical point needs to be computationally estimated; in particular, as usually done in finite-size scaling analyses, σ_c is estimated as the value of σ such that the variance of the order parameter R is maximal [5, 13]. As can be seen in Fig.1a and Fig.1b, showing results of our computer simulations for a system of $N = 500$ units, the critical point is located at $\sigma_c \approx 0.98$ (and shifts progressively towards 1 as N is increased). Observe that at the estimated critical point, owing to finite-size effects, the level of synchronization is $R \simeq 0.2$. This is illustrated in Fig.1c, which shows three characteristic raster plots within the synchronous phase $\sigma = 0.9$, the critical point $\sigma_c(N = 500) \approx 0.98$ and the asynchronous phase $\sigma = 1.1$, respectively.

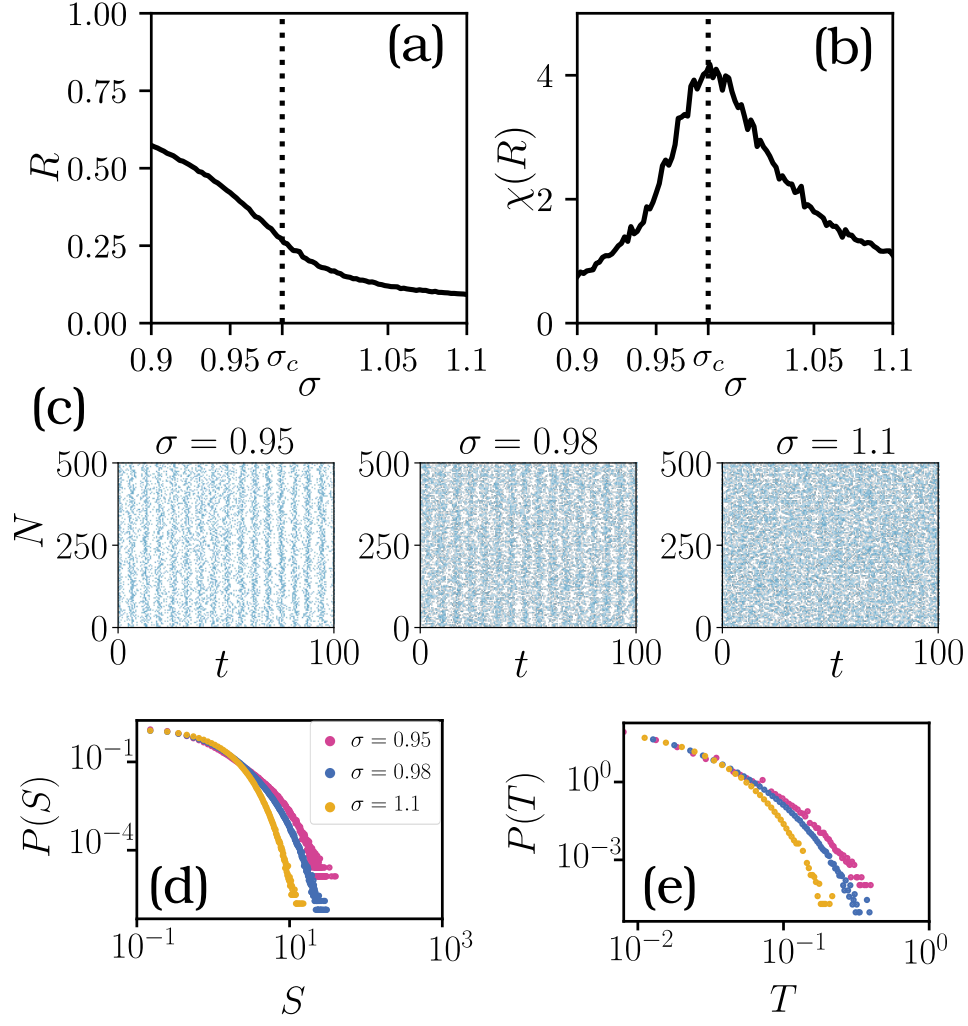


FIG. 1. **Avalanche statistics in the stochastic Kuramoto model on fully connected networks.** (a) Kuramoto order parameter (R) as a function of the noise intensity σ for a finite network size $N = 500$. (b) The Kuramoto critical point is defined as the point of maximum variance of the order parameter, χ , which occurs at $\sigma_c = 0.98$ (vertical dashed line). (c) Raster plots of the Kuramoto model at the synchronous phase ($\sigma = 0.95$, left plot), the critical point ($\sigma_c = 0.98$, central plot) and the asynchronous phase ($\sigma = 1.1$, right plot). (d) Distributions of size events in the three phases for the same representative values of σ as above. (e) Distribution of time events in all the three phases for the same parameter values. Let us underline the lack of power-law distributions at criticality, i.e. when the system undergoes a collective Hopf bifurcation. Parameter values: $\omega = 1$ and $J = 1$.

As an important technical remark, we should emphasize that in numerical simulations of the stochastic Kuramoto model, for any finite size N , the integration step δt needs to be small enough as to have sufficient time resolution, i.e. $\delta t < \Delta t = \langle \text{ISI} \rangle$, so that avalanches can be measured. Observe that this might depend on N ; in particular, in the asynchronous phase, as the number of neurons N grows, the $\langle \text{ISI} \rangle$ decreases, and thus one needs progressively smaller integration steps to measure avalanches. In the limit $N \rightarrow \infty$, the asynchronous raster plot has an average interspike interval $\langle \text{ISI} \rangle \rightarrow 0$ and, consequently, one could say that avalanches are not well defined if a fixed time bin was considered. On the other hand by considering sufficiently small δt 's for each case, our computational analyses –summarized in Fig. 1 panels (d) and (e)– show that the avalanche statistics do not exhibit heavy tails.

3. BIFURCATIONS IN THE SINGLE UNIT OF THE LANDAU-GINZBURG MODEL

The Landau-Ginzburg model [5] was pioneer in proposing that scale-free avalanches occur at the edge of a synchronization phase transition. It relies on a model for the dynamics of individual mesoscopic regions in the cortex. Each such region (or “unit”) is characterized by two dynamical variables: its level of (mesoscopic) neuronal activity $\rho(t)$ and the amount of available synaptic resources $R(t)$. The dynamics (at a deterministic level, i.e. excluding fluctuations) is described by

$$\begin{cases} \dot{\rho}(t) = (R(t) - a)\rho + b\rho^2 - \rho^3 + h \\ \dot{R}(t) = \frac{1}{\tau_R}(\xi - R) - \frac{1}{\tau_D}R\rho \end{cases} \quad (1)$$

where $a, b > 0$ are constants, h is a very small external driving (that can be set to 0 in the absence of external stimuli), $\eta(t)$ is a zero-mean Gaussian white noise, and ξ is the maximum amount of available synaptic resources, which serves as a control parameter which regulates the system state. In the second equation τ_R and τ_D represent the time scales of recovery and depletion of synaptic resources, respectively.

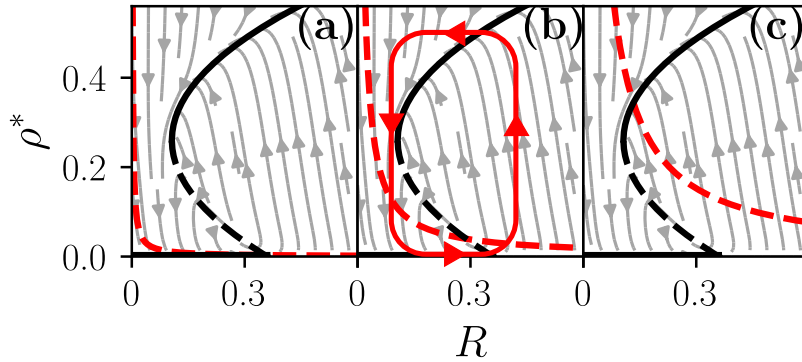


FIG. 2. **Nullclines of the single mesoscopic unit of the Landau-Ginzburg model 1.** Characteristic flow diagrams and nullclines of the Landau-Ginzburg mesoscopic unit, for three different values of ξ . The nullclines for the activity ρ (black lines) can display two types of solutions depending on the value of the available resources, R : up ($\rho \neq 0$ for large values of R), down ($\rho = 0$ for small values of R) and bistability between these two for intermediate values of R . Black dashed lines represent unstable fixed points ρ^* . Nullclines $\dot{R} = 0$ are represented by red dashed lines. For low values of the order parameter ξ , the only stable fixed point is the absorbing state $\rho^* = 0$ (black point). (b) When ξ is increased, the R -nullcline intersects the unstable branch of the ρ -nullcline, giving rise to a limit cycle (red solid line). (c) When ξ is large enough, the up-state fixed point becomes the only stable solution.

Observe that the equation for the activity ρ —assuming the amount of synaptic resources R is fixed—is the minimal form of a first-order phase transition with hysteresis (or saddle-node bifurcation). It displays a quiescent (or “down”) state $\rho = 0$ when $R \leq a$, and an active or “up” state for $R > a$. On the other hand, the second equation accounts for the dynamics of the level of synaptic resources, and includes a slow charge/recovery term (dominating when activity is low) and a fast discharge/consumption, which dominates the dynamics in the presence of activity, $\rho \neq 0$.

A simple analysis of Eqs.(1) shows that the system behavior depends on the value of the maximum allowed synaptic resources, ξ (see Fig. 3). If $\xi < a$, the only fixed point is a quiescent state of low activity. For larger values of ξ , the two nullclines of Eq.(1) intersect at an unstable fixed point, giving rise to a limit cycle, i.e. to *relaxation oscillations* in which both $\rho(t)$ and $R(t)$ oscillate. Finally, if ξ is large enough, an up state (fixed point with non-vanishing activity) emerges. For more details we refer to [5] and [15].

Fig.3 illustrates the bifurcation diagram of Eq.(1) as the control parameter ξ is varied. In agreement with what just described, values $\xi < a$ leads to a “down” steady state with vanishing activity and non-depleted synaptic resources, i.e. $R = \xi$. At $\xi_c = a$ there is an *infinite-period homoclinic bifurcation* into a limit cycle. In order to determine if this bifurcation is homoclinic or rather a saddle-node into an invariant circle (SNIC) one, we have explicitly measured the average period between oscillations and plotted against the control parameter. The result displays a logarithmic decay of the period (see Fig. 3b), which is a typical feature of homoclinic bifurcations [14]. Finally, as the control parameter is further increased one encounters another homoclinic bifurcation at which the limit cycle disappears, giving rise to an “up” fixed point.

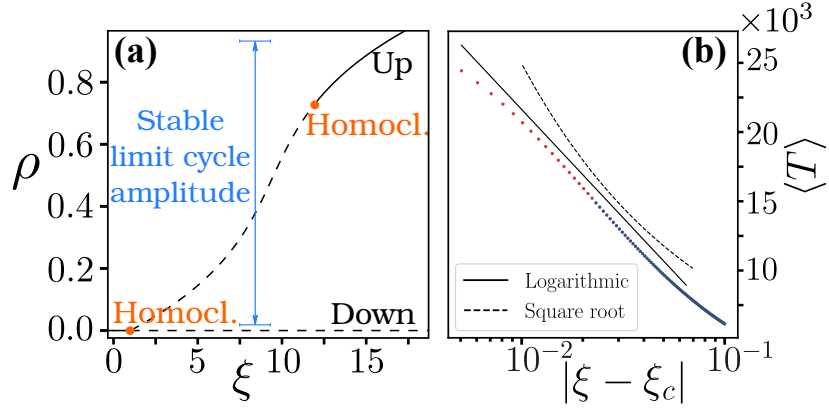


FIG. 3. **Bifurcations of the single unit dynamics of the Landau-Ginzburg model.** Stable fixed points of Eq.(1) are represented as a continuous line, while unstable ones correspond to dashed lines. Parameters: $a = 1.0$, $b = 1.5$, $\tau_R = 10^3$, $\tau_D = 10^2$, $h = 0$. (a) As the control parameter ξ is increased, the down-state fixed point loses its stability via a homoclinic bifurcation. (b) Period of oscillations as a function of the control parameter ξ . The set of equations 1 was integrated for a fixed long time in order to compute the period as the average time between spikes (jumps to the up branch). Points marked in red indicate that the number of spikes used for computing the average period were relatively low (because of costly statistics). Note that as $\xi \rightarrow \xi_c$, larger simulations are required (increasing integration error). The data are much better fitted by a logarithm (characteristic of homoclinic bifurcations) than by a square-root fit (characteristic of SNIC bifurcations) [14]. All numerical solutions are found using Wolfram Mathematica.

4. A NOTE ON DIFFERENT TYPES OF EXCITABILITY AND BIFURCATIONS

A system is defined as *excitable* when it presents a single, stable equilibrium, but a sufficiently strong input is able to drive the system in a large excursion in the phase space, before returning later to the stable fixed point [16–18]. Many physical and biological systems exhibit excitability [17]. Excitability is a concept of special importance in the context of neuroscience, where neurons are at rest, and a super-threshold signal is able to evoke a large response (e.g. a spike), returning at the end to the resting state. Different types of neurons may respond in different ways to the same input, leading to the so called “excitability classes” [16, 18]. The most usual classes are excitability classes I and II [16].

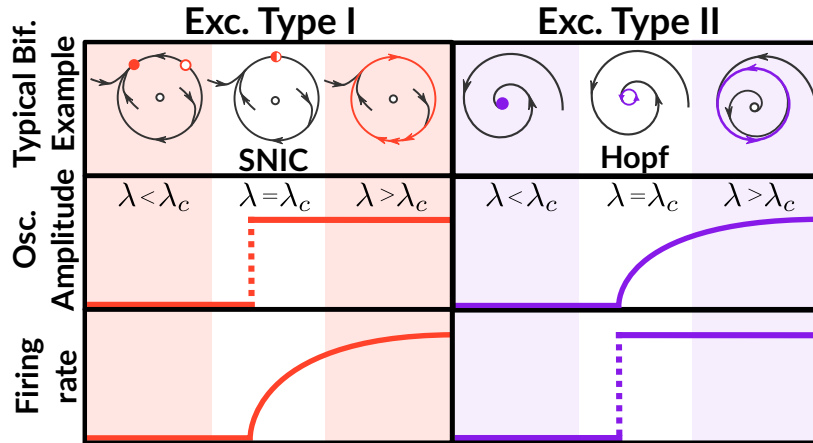


FIG. 4. **Excitability and bifurcations.** Side-by-side comparative sketch of infinite-period (SNIC) and Hopf bifurcations, which are representative examples of type-I and type-II excitability, respectively. Note that the firing rate is directly related with frequency of oscillations: vanishingly-small firing rates correspond to arbitrarily large firing frequencies.

Type-I excitability is characterized by a continuous growth of the spiking rate when the input current is continuously increased, while *Type-II excitability* involves a sudden jump in the spiking rate under the same circumstances. In bifurcation theory, type-I excitability corresponds to situations where the corresponding limit cycle appears with a

vanishing frequency, i.e. infinite-period bifurcations, while in type-II excitability limit cycles emergence with a finite, non-vanishing frequency [16].

Two representative examples of bifurcations corresponding to classes I and II are the SNIC and Hopf bifurcation, respectively, as sketched in Fig. 4. The homoclinic bifurcation is common in neuronal models [19], and belongs to class I neuronal excitability, as the SNIC bifurcation. Both are differentiated only by the critical exponents of the firing rate. A comprehensive summary of the relationship between excitability classes and bifurcations can be found, for example, in [20].

It should be noted that the mean-field phase diagram described in the main text includes these two main types of excitability near the bistability region, where the system behaves as collectively excitable. The bistability region is surrounded by other types of bifurcations such as saddle nodes as well as *codimension-2 bifurcations*, where lines of standard (codimension-1) bifurcations intersect. Codimension-2 points, which in our case include Bogdanov-Takens, saddle-node-loop and cusp bifurcations can display richer dynamics [16, 19, 21, 22]).

We have classified synchronization transitions using a nomenclature that resembles that of excitability classes. In type-I synchronization, oscillations emerge at the transition point with zero frequency (infinite period) and finite amplitude, while in type-II synchronization, oscillations are born with a fixed non-vanishing frequency. The phenomenology becomes richer in "hybrid-type" synchronization transition, where the co-dimension 2 bifurcations and bistability are present.

5. MATHEMATICAL ANALYSIS OF GLOBALLY COUPLED OSCILLATORS

In order to assess the collective behavior of the system of coupled oscillators, here we reproduce with detail the derivation of the equations for the order parameter and discuss different closure methods. Most of these calculations can be found in the literature but, for the sake of clarity, we reproduce them here in a self-consistent way. Our model is described by the set of stochastic equations,

$$\dot{\varphi}_j = \omega + a \sin \varphi_j + \frac{J}{M_j} \sum_{i \in n.n.j}^{M_j} \sin(\varphi_i - \varphi_j) + \sigma \eta_j(t). \quad (2)$$

It is convenient to remove one parameter, fixing e.g. $\omega = 1$. Here, we also set $J = 1$, leaving a and σ as the only free parameters. For completeness we verify a posteriori that results are robust to changes in J (SI-6).

5.1. Order-parameter equations

Equation (2) is very similar to the previously discussed stochastic Kuramoto model, with the exception of the additional term $a \sin(\varphi)$ which induces an inhomogeneity in angular velocity across the unit circle of each oscillator. As discussed in SI-7 (in particular, in Section 7.7.1), such an inhomogeneity makes the Kuramoto parameter inadequate to characterize the phase diagram of the present model as, for $a \neq 0$, there is a particular phase value around which each individual oscillator tends to spend most of the time. For uncoupled oscillators this occurs for $\varphi = \pm \arcsin(\omega/a)$ where the angular velocity is minimal; this heterogeneity in angular velocity leads to a non-vanishing value of the Kuramoto order parameter, even in the case when oscillators are uncoupled or, more in general, when they are asynchronous.

In order to circumvent this problem analytically, it is possible to consider the hierarchy of higher-order moments of the variable $e^{i\varphi}$, i.e. the so-called Kuramoto-Daido parameters, Z_k :

$$Z_k = \langle e^{ik\varphi} \rangle \equiv \frac{1}{N} \sum_{j=0}^N e^{ik\varphi_j} \equiv R_k e^{i\psi_k} \quad (3)$$

where $k = 1, 2, \dots, \infty$ and of which the Kuramoto order parameter Z_1 is a particular case. For convenience, we will use either the notation in terms of amplitudes and phases (R_k and ψ_k) to represent the complex-valued Kuramoto-Daido parameters Z_k . Using standard trigonometric relations, Eq.(2) can be rewritten as a function of $Z_1(t) = R_1(t)e^{i\psi_1(t)}$, leading to the following set of Langevin equations,

$$\dot{\varphi}_j(t) = \omega + a \sin \varphi_j(t) + J R_1(t) \sin(\psi_1(t) - \varphi_j(t)) + \sigma \eta_j(t) \quad (4)$$

where the mean-field nature of the coupling is evident.

In order to solve these equations, we employ a standard procedure to deal with coupled oscillators [23–27]. The first step is to consider a large number of oscillators, $N \rightarrow +\infty$, so that the system can be described in the continuum limit using the probability density to find an oscillator around any given phase value φ , i.e. $P(\varphi)d\varphi$. The evolution of such a probability density is given by the Fokker-Planck equation

$$\partial_t P(\varphi, t) = \frac{\sigma^2}{2} \partial_\varphi^2 P(\varphi, t) - J \partial_\varphi \left[\left(\omega + a \sin \varphi + \frac{Z_1 e^{-i\varphi} + c.c.}{2i} \right) P(\varphi, t) \right] \quad (5)$$

where the identity $R_1 \sin(\psi_1 - \varphi) = (Z_1 e^{-i\varphi} + \bar{Z}_1 e^{i\varphi})/(2i)$ has been used to simplify the forthcoming algebra. As the density $P(\varphi, t)$ is periodic in the angle variable, it can be expanded in Fourier series:

$$P(\varphi, t) = \frac{1}{2\pi} \sum_{k=-\infty}^{+\infty} p_k(t) e^{ik\varphi}, \quad (6)$$

and $p_k = \bar{p}_{-k}$, where the bar stands for complex conjugate. It turns out that the Kuramoto-Daido parameters coincide with these coefficients:

$$Z_k = \int_0^{2\pi} P(\varphi, t) e^{ik\varphi} d\varphi = p_k. \quad (7)$$

Plugging the series expansion (6) into the Fokker-Planck equation one obtains an infinite set of differential equations, one for each of the parameters Z_k , i.e. for the Kuramoto-Daido parameters Z_k (observe that, as $Z_{-k} = \bar{Z}_k$, it suffices to analyze the order parameters with $k \geq 0$). In order to obtain differential equations for each Z_k , note that after performing the derivatives and doing some algebra, all the terms can be written as $(2\pi)^{-1} \sum_k f(Z_k, Z_{k+1}, Z_{k-1}, \dots) e^{ik\varphi}$ for some function f . Then, since the exponentials $e^{ik\varphi}$ are the elements of the Fourier basis, we can identify all parameters mode by mode, leading to an equation for the evolution of each Kuramoto-Daido order parameter [26, 28]. The resulting set of equations,

$$\dot{Z}_k = Z_k \left(i\omega k - \frac{k^2 \sigma^2}{2} \right) + \frac{ak}{2} (Z_{k+1} - Z_{k-1}) + \frac{Jk}{2} (Z_1 Z_{k-1} - \bar{Z}_1 Z_{k+1}), \quad (8)$$

constitutes an exact description of the system.

As reported below, we solved Eq.(8) including up to $k = 50$ harmonics (i.e. imposing $Z_{51} = 0$) and monitored the order parameters (see Section 7.7.1). We found an excellent agreement with direct simulations, including the existence of a small bistable phase [24, 26], as shown in Fig. 2C of the main text. The exact location of the small bistable phase, however, is affected by finite-size effects in direct simulations.

In order to proceed analytically, given that all equations are coupled, one needs to find a sound dimensional reduction or “closure” to truncate the infinite hierarchy [27, 29]. Different closures have been proposed in the literature of coupled oscillators. In what follows we discuss three of them.

5.2. Approximate solutions or closures

In deterministic, noise-free systems, an exact solution to equation (8) is provided by the Ott-Antonsen ansatz [30], which consists in writing $Z_k(t) = [Z(t)]^k$, so that the first moment already contains all the relevant information. On the other hand, the situation is more complicated for stochastic systems for which the Ott-Antonsen ansatz does not provide an exact solution [27, 28]. In particular, using the Ott-Antonsen ansatz and writing $Z(t) = R(t)e^{i\psi(t)}$ leads to the system of equations

$$\begin{aligned} \dot{R} &= \frac{1}{2} R [J(1 - R^2) - \sigma^2] - \frac{1}{2} a (1 - R^2) \cos \psi, \\ \dot{\psi} &= \omega + \frac{a(1 + R^2) \sin \psi}{2R}. \end{aligned} \quad (9)$$

Remarkably, these equations are exactly the same as the ones obtained by Childs and Strogatz in the case of deterministic oscillators with heterogeneous (quenched) frequencies distributed as a Lorentzian [31]. However, only the

deterministic system is exactly solved by the Ott-Antonsen ansatz, while in the stochastic case it gives an approximation of order $\mathcal{O}(\sigma^2)$ [28].

In order to increase the precision of the closure, one can assume that the global phase is distributed as a (wrapped) Gaussian with some mean $\psi(t)$ and variance $\Delta(t)$ [26]:

$$P(\varphi, t) = \frac{1}{\sqrt{2\pi\Delta}} \sum_{k=-\infty}^{+\infty} \exp \left[-\frac{(\psi - \varphi + 2\pi k)^2}{2\Delta} \right] \quad (10)$$

The Kuramoto-Daido parameters can be explicitly computed via direct integration,

$$Z_k(t) = \int d\varphi P(\varphi, t) e^{ik\varphi} = e^{-\frac{1}{2}k^2\Delta(t)} e^{ik\psi(t)}. \quad (11)$$

Plugging this ansatz into Eq.(8) leads to

$$\dot{\psi}(t) = \omega + ae^{-\Delta/2} \cosh \Delta \sin \psi, \quad (12)$$

$$\dot{\Delta}(t) = \sigma^2 + 2 \sinh \Delta \left(ae^{-\Delta/2} \cos \psi - J e^{-\Delta} \right). \quad (13)$$

Observe that Eq.(11) allows one to write Z_k as a function of only the first mode [28], Z , giving a functional form very similar to the Ott-Antonsen ansatz:

$$Z_k = |Z|^{k^2-k} Z^k \quad (14)$$

Let us remark that, actually, the Ott-Antonsen ansatz is equivalent to the assumption of a Lorentzian distribution for the angles. That is, changing Eq.(10) to a Lorentzian distribution and following the same procedure one recovers the Ott-Antonsen ansatz. The wrapped Gaussian approximation is slightly superior to the Ott-Antonsen one, but, as we will see shortly, it is not good enough as to generate a precise phase diagram (see Fig. 6 below for a comparison).

A way to go beyond the Ott-Antonsen and the Gaussian ansatzs is to take into account more harmonics in the expansion. Tyulkina et al [27, 28] proposed to use the circular cumulants of the order parameters to generate a better closure. The advantage of the cumulant expansion is that all cumulants, except $\chi_1 = Z$, vanish when the Ott-Antonsen ansatz is selected, so choosing additional non-zero cumulants gives rise to systematic corrections to the Ott-Antonsen solution, order by order in such an expansion. In particular, the first three cumulants are given by $\chi_1 = Z$, $\chi_2 = Z_2 - Z^2$, $\chi_3 = (Z_3 - 3ZZ_2 + 2Z^3)/2$. Selecting Z and χ_2 to be different from 0 but fixing $\chi_3 = 0$ gives $Z_3 = Z^3 + 3Z\chi_2$, effectively closing the infinite system [32]. Substituting this last in the equation for the first three harmonics, the resulting system reads:

$$\begin{aligned} \dot{Z} &= \frac{1}{2} (J - \sigma^2 + 2i\omega) Z + a (Z^2 - 1 + \chi_2) - J (Z|Z|^2 + \chi_2 \bar{Z}), \\ \dot{\chi}_2 &= 2\chi_2(i\omega + aZ) - \sigma^2(2\chi_2 + Z^2) - 2J\chi_2|Z|^2. \end{aligned} \quad (15)$$

Note that imposing $\chi_2 = 0$ leads to the Ott-Antonsen ansatz, as expected. This closure provides us with a noticeable quantitative improvement on where the Hopf and SNIC bifurcations are located, which coincide very well with the results of numerical integrations. On the other hand, this approximation does not lead to the regime of bistability, which is found in numerical simulations of the system. Losing the possibility of bistability in analytical approaches relying on closures is a well-known problem in stochastic processes [29].

6. BIFURCATION ANALYSIS OF THE OTT-ANTONSEN EQUATIONS

In order to gain analytical insight into the structure and topological organization of the phase diagram, here we analyse the bifurcation diagram of the approximation provided by the simpler Ott-Antonsen closure, eqs. (9), i.e.:

$$\begin{aligned} \dot{R} &= \frac{1}{2} R [J (1 - R^2) - \sigma^2] - \frac{1}{2} a (1 - R^2) \cos \psi, \\ \dot{\psi} &= \omega + \frac{a (1 + R^2) \sin \psi}{2R}. \end{aligned} \quad (16)$$

Observe first that, for a fixed value of R , the equation of the collective phase ψ is the normal form of a saddle-node into an invariant circle (SNIC) bifurcation. On the other hand, the equation for \dot{R} is almost the same as in the Kuramoto model, but adding a perturbation proportional to the “excitability parameter” a . The above system of equations is difficult to study analytically, but its bifurcations can be obtained following the same procedure of Childs and Strogatz who studied this system with a fixed value of $\sigma = \sqrt{2}$ [31].

The main idea is as follows: in the Kuramoto limit ($a = 0$) the system undergoes a Hopf bifurcation; on the other hand, individual (uncoupled) oscillators, i.e. for $J = 0$, exhibit a SNIC bifurcation. Hence, by continuity in solutions, we expect two branches of these two types of bifurcations to be present in Eq.(9).

Calling Q the Jacobian at a fixed point, at Hopf bifurcations $\text{tr } Q = 0$ while in a saddle-node $\det Q = 0$ [14]. Thus, imposing one of these conditions, together with the fixed point equations $\dot{R} = \dot{\psi} = 0$, leads to a set of equations for the parameters of the system as a function of the fixed point values, R^* and ψ^* . Since such values are bounded, one can use these equations as parametric equations of the bifurcation curve, without having to compute explicitly the values of the fixed points and their stability.

Let us start with the Hopf bifurcation. Between parameters and fixed points, there are 6 unknowns: R^* , ψ^* , ω , a , J and σ . Remember that in the simulations we fixed $\omega = J = 1$ to leave a and σ as the only free parameters. In what follows, we obtain equations for the bifurcations, written in a parametric form $a = a(R^*, \psi^*, \omega, J)$ and $\sigma = \sigma(R^*, \psi^*, \omega, J)$. After some algebra, it turns out that not all the dependences are necessary. Solving for $\dot{R} = \dot{\psi} = \text{tr } Q = 0$, there are 3 remaining parameters. We can choose any parameters to solve for, but it turns out (as shown in [31]) that solving for R , $\cos \psi$ and $\sin \psi$ is extremely convenient. Note that these are only two parameters, since the sine and cosine are not independent function as $\sin^2 \psi + \cos^2 \psi = 1$. Of course, one could have tried to directly solve for ψ and a , but it is easier to obtain expressions for the trigonometric functions and then extract a :

$$a_H = \sqrt{\frac{J - \sigma^2}{J + \sigma^2} \frac{\sqrt{4\omega^2(J + \sigma^2)^2 + J^2(J - \sigma^2)^2}}{2J}} \quad (17)$$

Note that, in this case, we obtained a parametric curve for the Hopf bifurcation, $a_H = a_H(\omega, J, \sigma)$, without requiring specific knowledge about the location of the fixed points. In particular, as J is kept fixed, it is possible to derive a curve $a_H = a_H(\omega, \sigma)$.

In what respects saddle-node bifurcations, the calculation is a bit more involved, since solving for the same 3 variables gives high-degree polynomials for R that cannot be explicitly solved. For this reason, we choose to solve for ω , $\cos \psi$ and $\sin \psi$, since in this way the parameters do not depend on ψ . After solving and simplifying the resulting equations, one obtains:

$$\begin{aligned} \omega_S &= \frac{(1 + R^2)^{3/2}}{2(1 - R^2)^2} \sqrt{J(1 - R^2)(2\sigma^2 - J(1 - R^2)^2) - \sigma^4(1 + R^2)}, \\ a_S &= \frac{\sqrt{2}R^2}{(1 - R^2)^2} \sqrt{(J(1 - R^2) - \sigma^2)(2\sigma^2 - J(1 - R^2)^2)}. \end{aligned}$$

Since $0 \leq R \leq 1$, and one needs to explore all the possible fixed points, there are actually two free parameters to choose. Given that J is kept fixed in our simulations, we dismiss it and obtain ω and a as functions of σ .

The manifolds of Hopf and SNIC bifurcations could be drawn together in a three-dimensional space, using ω , a and σ as coordinates. An alternative easy way to visualize them is to make projections into the (a, σ) two-dimensional space for different values of J (see Fig. 5). Since we set $\omega = 1$, and in each such projection J is fixed, the Hopf bifurcation is then obtained as $a_H = a_H(\sigma)$, while the saddle node is obtained by solving Eqs.(18) as a parametric curve, depending on R and σ . Fig. 5 clearly shows that, for different values of J , there is a bistability region delimited by a Hopf line and two saddle-node lines. This region decreases in size as the coupling decreases, until it disappears for sufficiently low values of J .

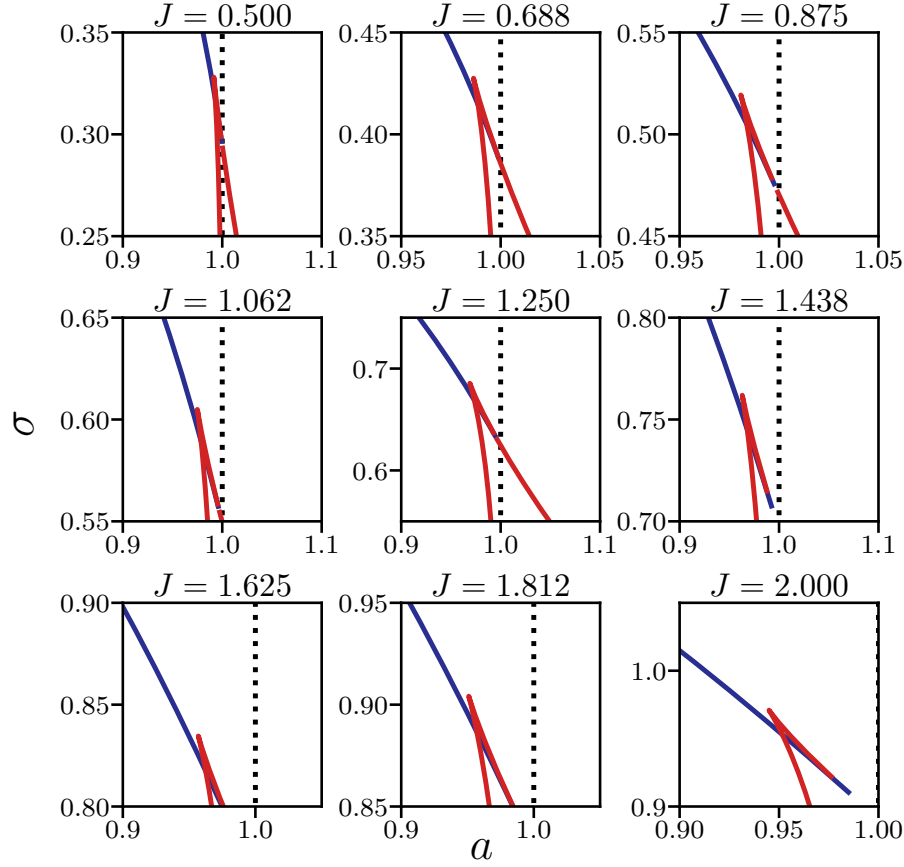


FIG. 5. **Bifurcations in the Ott-Antonsen approximation.** Representation of the solutions of the equations (17) and (18) for different values of the coupling constant J . Blue lines describe branches of Hopf bifurcations, while the red lines correspond to saddle- bifurcations. All the graphs, for different values of J , are zooms made to underline the existence of a region surrounded by the Hopf bifurcation (blue line) on the one side and saddle node bifurcations (red lines) on the others. Such a region is important as it describes a regime of bistability: all the selected values of J display a small bistable region, whose size decreases with J .

7. COMPUTATIONAL ANALYSES AND RESULTS

7.1. Phase diagram of the full model

As we have seen, deriving analytically all the phases and transitions between them is a difficult task and, thus, one needs to resort to computational analyses. First of all, an adequate order parameter needs to be defined. As discussed above, the usual Kuramoto order parameter, $R = |Z|$, is not a good choice for inhomogeneous oscillators, owing to the fact that $|\langle Z \rangle_t| \neq 0$ even when they are uncoupled or asynchronous, due to the different amount of time they spend at diverse phase values.

We employed the so-called Shinomoto and Kuramoto (SK) parameter that solves this problem, being able to discriminate between synchronous and asynchronous regimes [23]. In particular, we consider the –computationally more efficient– variant of such a parameter employed by Lima and Copelli [33]:

$$S = \sqrt{|\langle |Z|^2 \rangle_t - |\langle Z \rangle_t|^2}. \quad (18)$$

to distinguish the synchronized phase ($S \neq 0$) from asynchronous or excitable states ($S = 0$).

The main result of our computational analyses is the phase diagram reported in Fig. 1 of the main text. The different phases are identified computationally as follows:

- the synchronous region is characterized by a non-vanishing S value;

- the asynchronous and “collective excitability” regions are both characterized by $S = 0$. To detect this second regime one needs to perturb the system and analyze its collective response (or lack of it).
- The regime of bistability is difficult to study numerically since in finite networks, fluctuations can drive the system to jump between the two coexisting states. In order to determine this region, the analytical solution was computed by solving for the first 50 terms in the series expansion (8) and then it was computationally verified that, for large enough network sizes, two alternative stable states exist within such a region.

7.2. Accuracy of different closures

For the sake of completeness, we checked the accuracy of the different considered closures by comparing them with the results of computational analyses. In order to do so, the different ansatzs or closures: (i) the Ott-Antonsen (eqs. (9)), (ii) the Gaussian closure (eqs. (13)), and (iii) the Tyulkina *et al.* equations (eqs. 15) were solved near the Hopf and SNIC bifurcation branches and compared the results –shown in Fig. 6– with those of direct simulations of Eq.(2) as reported above. We would like to remark that, up to our knowledge, it is the first time that the accuracy of the different closures to locate different kind of bifurcations has been formally checked.

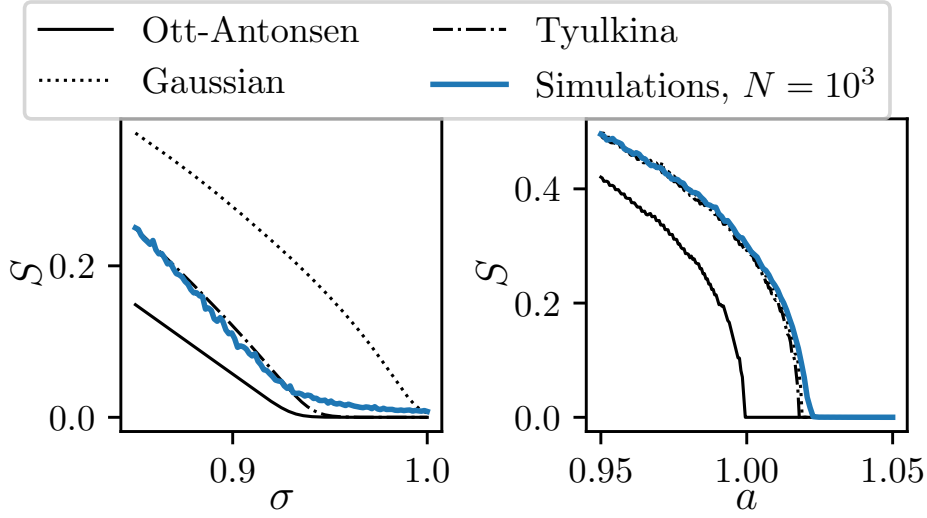


FIG. 6. **Comparison between the results obtained for analytical closures and direct simulations.** Shinomoto-Kuramoto parameter S along the Hopf and SNIC bifurcations, as measured both in simulations and numerical solutions obtained from different closures (as specified in the legend). Parameters: $\omega = J = 1$. Hopf, $a = 0.5$. SNIC, $\sigma = 0.275$. Direct simulations are performed in a fully connected network of size $N = 10^3$ (see Section 7.3 for computational details.)

The conclusion is that the ansatz by Tyulkina *et al.* [27] fits more accurately both the Hopf and SNIC branches than the other ones. The Gaussian ansatz captures very well the phenomenology near the SNIC bifurcation but not near the Hopf one. On the other hand, the Ott-Antonsen solution does not predict the transition accurately at any of the bifurcations. However, the ansatz by Tyulkina *et al.* [27] is not able to predict the existence of the bistability phase, while the other two do so. Solving the complete system of equations for the Kuramoto-Daido parameters, at least 5 harmonics are needed in order to find the bistability region.

7.3. Avalanches at different types of bifurcations

Here, we further investigate whether scale-free avalanches emerge when we moved away of the bistability region. Results at the different type of bifurcations are reported in Fig. 2 of the main text, which displays raster plots computed at either a (Type II) Hopf (upper panels) or at a (Type I) SNIC bifurcation point (lower panels), respectively, as well as within the synchronous and asynchronous phases surrounding them. Here, we show results for values slightly below, at and above the bifurcation. As discussed at extent in the main text, scale-free avalanches (with power-law distributed sizes and durations) emerge only in the vicinity of the hybrid type synchronization transition; when the

system is moved away from it, scaling behavior as well as scale-free behavior breaks down (see Fig. 7), while near the bistability region scale-free distributed avalanches remain (see Fig. 8).

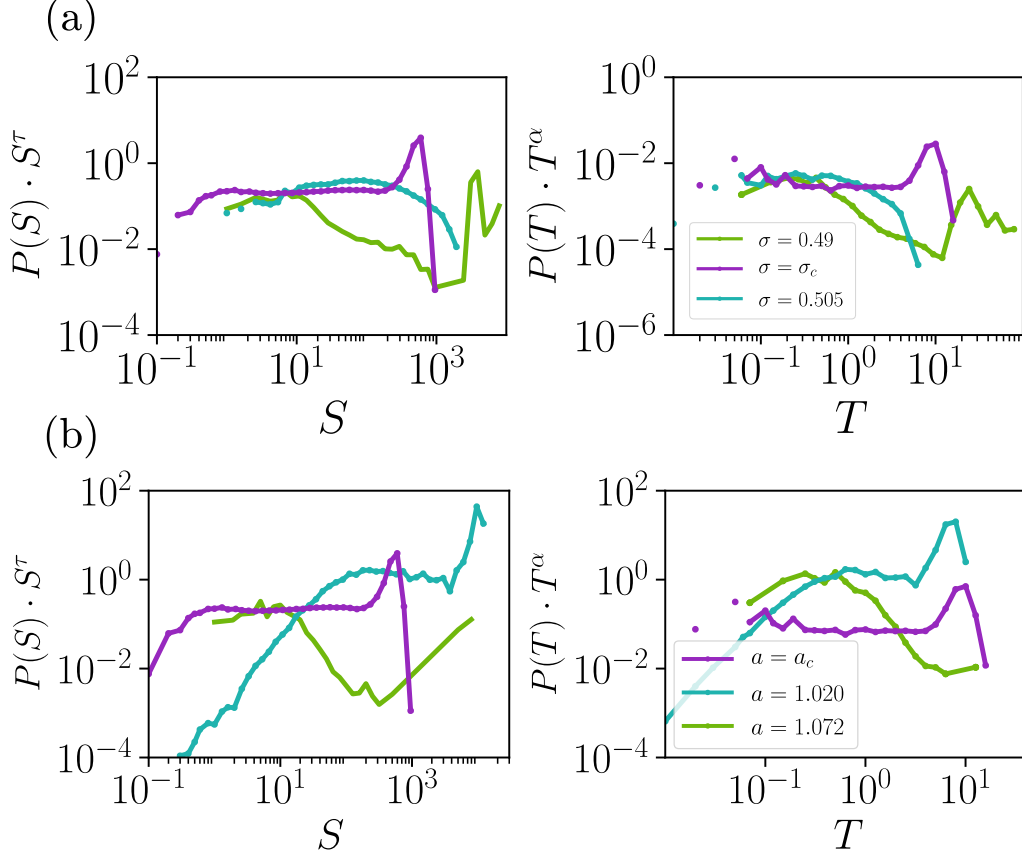


FIG. 7. **Avalanches at and away from the hybrid type synchronization transition.** (a) Avalanche-size and avalanche-duration distributions for a network of size $N = 5000$ evaluated at the hybrid type synchronization transition ($a = 1.07$, $\sigma_c = 0.496$) and two other nearby points, slightly away from it. The Figure includes: (a) avalanche-size and duration distributions for several values of the noise intensity σ (see legend) with fixed $a_c = 1.07$ and (b) avalanche-size and duration distributions for several values of the excitability a (see legend) keeping $\sigma_c = 0.496$ fixed. Power law behavior is observed only at the hybrid type transition

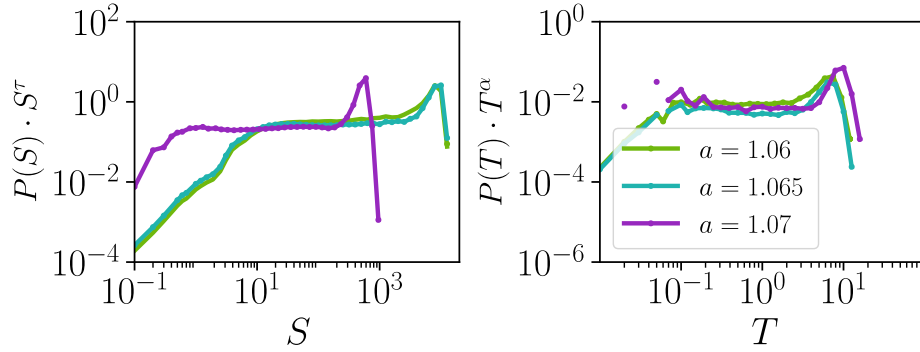


FIG. 8. **Avalanches close to the hybrid type synchronization transition** Avalanche-size and avalanche-duration distributions for a network of size $N = 5000$ evaluated at the hybrid type synchronization transition ($a = 1.07$, $\sigma_c = 0.496$) and two other nearby points, slightly to the left of it. Power law behavior is observed only in the bistable region close to the hybrid-type synchronization

On the contrary, careful inspection of the HT transition reveals that there exists a point at which we find clean scale-invariant avalanche distributions spanning across many decades and obeying finite-size scaling, so that the cutoffs of avalanche distributions increase in a scale-invariant way upon enlarging the system size (see main text and Fig.9b). Also, we show the scaling for the exponent γ , showing a value $\gamma^{-1} \approx 0.75(5)$ (see Fig. 9a). We observed a very similar phenomenology on 2D lattices, in which $\gamma^{-1} \approx 0.75(5)$. In both cases, the scaling relation linking these exponents, which is a crucial signature of criticality is satisfied.

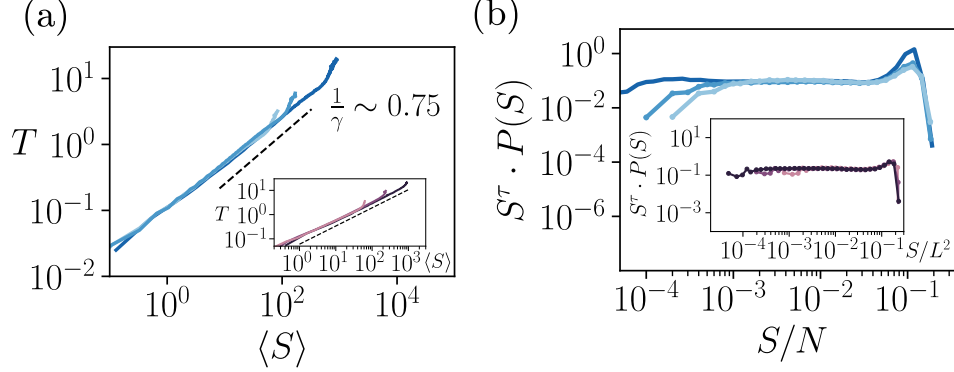


FIG. 9. **Exponents accuracy analysis** (a) Averaged avalanche size as a function of the duration for different system sizes. **Insets:** As in the main Figure, but for simulations in a 2D lattice for different system sizes. (b) Distribution of avalanche sizes multiplied by s^τ to obtain an asymptotically flat curve (to ease visual inspection of scaling) and re-scaled as a function of the system size to collapse the different curves. As expected from true scale invariance, avalanches become flat and collapse for the different system sizes. **Parameters at the hybrid transition synchronization** (a, σ) for fully connected networks, $N = 500$: (1.07, 0.520), $N = 1000$: (1.07, 0.505), $N = 5000$: (1.07, 0.496) and 2D networks, $L = 16$: (0.995, 0.192), $L = 32$: (0.982, 0.190), $L = 64$: (0.98, 0.185), $J = \omega = 1$. Dashed lines are guides to the eye showing the value of the fitted exponents.

7.4. Dynamical variability

As a complementary measure of complexity at the different transition points, we have also computed the probability distribution of the inter-spike intervals (ISI), along with its associated coefficient of variation (CV)

$$CV = \langle \sigma_{\text{ISI}} / \mu_{\text{ISI}} \rangle \quad (19)$$

where μ_{ISI} and σ_{ISI} are the mean and standard deviation of the inter-spike interval for each oscillator, respectively, [34] and $\langle \cdot \rangle$ indicates an average over units. For a Poisson process, one expects an exponential distribution of ISI's along with a $CV = 1$; as a rule of thumb, $CV > 1$ is the fingerprint of irregular spiking activity. Fig.10 shows the probability distribution of the ISIs, as well as the CVs for the different phases and transitions, as determined in computational analyses.

Only two cases exhibit $CV > 1$: the hybrid type synchronization transition, as well as a small neighborhood around it in the bistable regime; they are also the only two cases characterized by a broad distribution of ISI values. Thus, a high level of variability –similar to that observed in the cortex– is only found in the region around the hybrid type synchronization transition, but not in the neighborhood of either standard Hopf or SNIC bifurcations.

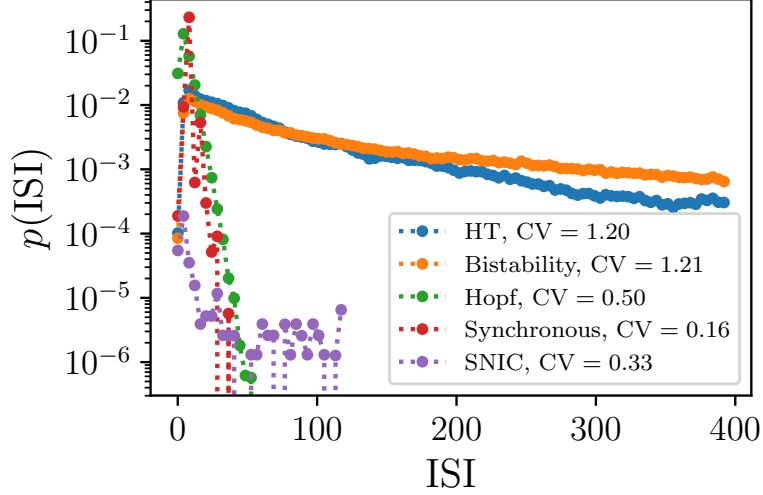


FIG. 10. **ISI distributions and CVs for a fully connected networks.** Probability distributions for inter-spike intervals (ISI) for different phases and bifurcations as shown in the legend. The coefficients of variation for each case are indicated also in the legend. Parameter values: Synchronous regime, $\sigma = 0.5$, $a = 0.5$; Hopf bifurcation, $a = 0.5$, $\sigma = 0.92$; collectively excitable phase, $\sigma = 0.5$, $a = 1.12$; hybrid type synchronization transition: $\sigma = 0.5$, $a = 1.07$; bistable regime: $\sigma = 0.5$, $a = 1.072$. Network size $N = 5000$.

8. PHASE DIAGRAM FOR THE MODEL ON TWO-DIMENSIONAL LATTICES

Computational analyses in 2D systems reveal a very similar phase diagram to the mean-field one, but with a richer phenomenology (as graphically illustrated in Fig.11). In a nutshell, there are three main phases, a asynchronous regime, an asynchronous one, and a collectively excitable phase, much as in the mean-field case. In the asynchronous regime, clusters of activity appear, propagate, and vanish dynamically, with an averaged constant level of network activation (smaller/larger close to the SNIC/Hopf transition, respectively) but with no overall synchronization. On the other hand, within the synchronous phase, activity wane and washes, and periods of overall quiescence are followed by bursts of overall activity that spreads quickly from different focuses. Such a collective propagation requires some level of synchronization [35]. Finally, the excitable state has all units in the “down” regime, with almost no activity, but is susceptible to respond to external perturbations or inputs.

Let us discuss the observed phenomenology at the different bifurcation lines separating these phases:

(i) Nearby the type-I synchronization transition, at the SNIC bifurcation (slightly within the synchronous phase) there is oscillating activity, that appears in the form of travelling waves. Visual inspection reveals, e.g. the presence of typical spiral patterns typical of two-dimensional excitable systems (see Supplementary videos and Fig.11 upper row).

(ii) Nearby the type-II synchronization transition, at the Hopf bifurcation (slightly within the synchronous phase) the overall level of activity oscillates in time (i.e. the system “breathes”) and is spatially distributed in fragmented clusters (see Fig.11, central row).

(iii) Near the hybrid type synchronization transition, the dynamical behavior is much more complex: somehow in between the overall oscillatory behavior along the Hopf line and the emergence of wavefronts at the SNIC line (see Fig.11 bottom row).

Thus, even if we are not making an attempt to quantify spatio-temporal complexity here, it is clear that more complex dynamics emerge around the HT synchronization transition.

As shown in Fig.12 the computationally-obtained phase diagram in the case of two-dimensional lattices has a structure qualitatively identical to the mean-field case, including the same phases.

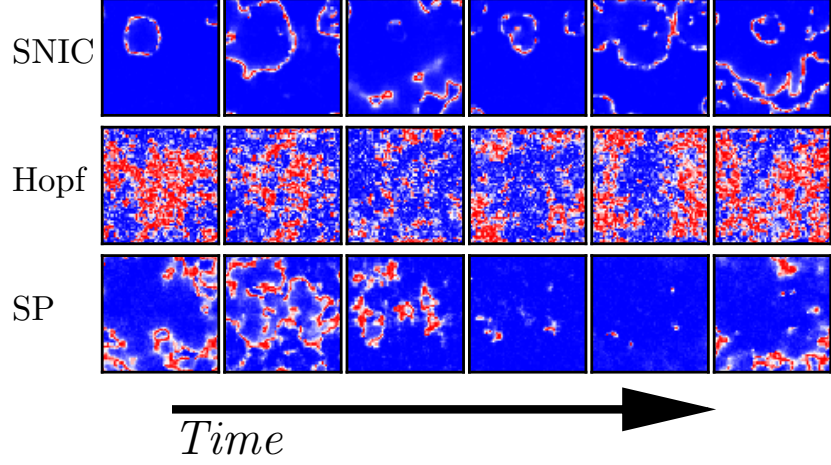


FIG. 11. **Spatio-temporal dynamics on two-dimensional systems** The figure shows three rows, each one with six different frames corresponding to six different times on a running simulation, for the following cases: Upper row: near the different bifurcations SNIC ($a = 1$, $\sigma = 0.08$); central row: near a Hopf bifurcation ($a = 0.5$, $\sigma = 0.65$); and lower row: hybrid type synchronization transition ($a = 0.98$, $\sigma = 0.185$). Blue color indicates lack of activity, while red color stands for maximum levels of activity (identified as $1 + \sin \phi_j$). Near the SNIC transition, noise fluctuations generate wave fronts that propagate in the system. At the Hopf transition there is some background activity whose level grows and shrinks in a periodic way. At the hybrid type synchronization transition the spatio-temporal patterns are more complex, being a mixture of the two previous types; in particular, the system falls sometimes in the excitable state. Simulations performed for $N = 64^2$ with periodic boundary conditions. Videos showing the evolution for both cases and the other phases can be found in the Supplementary Information.

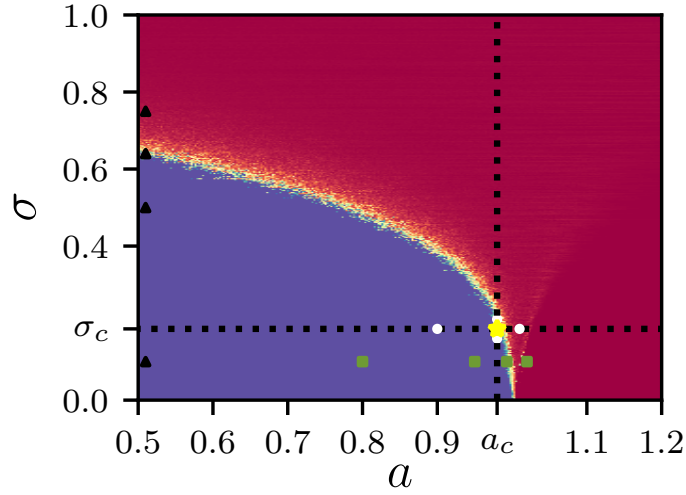


FIG. 12. **Phase diagram for a 2D lattice of coupled excitable oscillators** for different values of σ and a , using the Shinomoto-Kuramoto (SK) order parameter (color coded). Reddish colors stand for asynchronous states, while blueish colors correspond to partially synchronized ones. As in the FC-network case, the system can de-synchronize either through a supercritical Hopf bifurcation or through a SNIC bifurcation. In an intermediate region it is possible to find a hybrid type synchronization transition (yellow star). This is characterized as the point where power-law distributed avalanches obeying finite-size scaling appear. Symbols describe the coordinates for which Supplementary Videos were recorded: “Hopf” bifurcation (black triangles); “SNIC” bifurcation (green squares) and the HT transition point (white circles and yellow star).

REFERENCES

- [1] J. M. Beggs and D. Plenz, *J. Neurosci.* **23**, 11167 (2003).
- [2] D. Plenz and E. Niebur, *Criticality in Neural Systems* (John Wiley & Sons, New York, 2014).
- [3] G. Hahn, T. Petermann, M. N. Havenith, S. Yu, W. Singer, D. Plenz, and D. Nikolić, *J. Neurophysiol.* **104**, 3312 (2010).
- [4] A. J. Fontenele, N. A. de Vasconcelos, T. Feliciano, L. A. Aguiar, C. Soares-Cunha, B. Coimbra, L. Dalla Porta, S. Ribeiro, A. J. Rodrigues, N. Sousa, *et al.*, *Phys. Rev. Lett.* **122**, 208101 (2019).
- [5] S. di Santo, P. Villegas, R. Burioni, and M. A. Muñoz, *Proc. Natl. Acad. of Sci. U.S.A.* **115**, E1356 (2018).
- [6] M. Benayoun, J. D. Cowan, W. van Drongelen, and E. Wallace, *PLoS Comput. Biol.* **6**, e1000846 (2010).
- [7] S. Yu, A. Klaus, H. Yang, and D. Plenz, *PloS one* **9**, e99761 (2014).
- [8] E. Montbrió, D. Pazó, and A. Roxin, *Phys. Rev. X* **5** (2015).
- [9] V. Priesemann, M. H. Munk, and M. Wibral, *BMC neuroscience* **10**, 1 (2009).
- [10] A. Levina and V. Priesemann, *Nat. Comm.* **8**, 1 (2017).
- [11] J. Wilting and V. Priesemann, *Nat. Comm.* **9**, 2325 (2018).
- [12] Observe that the parameter ω is not relevant as a change of variable to co-rotating reference frame can be used to set $\omega = 0$.
- [13] J. A. Acebrón, L. L. Bonilla, C. J. Pérez Vicente, F. Ritort, and R. Spigler, *Rev. Mod. Phys.* **77**, 137 (2005).
- [14] S. H. Strogatz, *Nonlinear Dynamics and Chaos: With Applications to Physics, Biology, Chemistry, and Engineering*, Studies in Nonlinearity (Addison-Wesley Pub, Reading, Mass, 1994).
- [15] V. Buendía, S. di Santo, P. Villegas, R. Burioni, and M. A. Muñoz, *Phys. Rev. Res.* **2**, 013318 (2020).
- [16] E. M. Izhikevich, *Dynamical Systems in Neuroscience: The Geometry of Excitability and Bursting* (The MIT Press, Cambridge, 2006).
- [17] B. Lindner, J. García-Ojalvo, A. Neiman, and L. Schimansky-Geier, *Phys. Rep.* **392**, 321 (2004).
- [18] S. A. Prescott, in *Encyclopedia of Computational Neuroscience*, edited by D. Jaeger and R. Jung (Springer New York, New York, NY, 2014) pp. 1–7.
- [19] J.-H. Schleimer, J. Hesse, and S. Schreiber, *arXiv:1902.00951* (2019), *arXiv:1902.00951 [q-bio]*.
- [20] Z. Zhao and H. Gu, *Sci. Rep.* **7**, 1 (2017).
- [21] J. D. Cowan, J. Neuman, and W. van Drongelen, *J. Math. Neurosci.* **6**, 1 (2016).
- [22] J. Hesse, J.-H. Schleimer, and S. Schreiber, *Phys. Rev. E* **95** (2017).
- [23] S. Shinomoto and Y. Kuramoto, *Prog. Theor. Phys.* **75**, 1105 (1986).
- [24] S. Shinomoto and Y. Kuramoto, *Prog. Theor. Phys.* **75**, 1319 (1986).
- [25] A. Pikovsky, M. Rosenblum, and J. Kurths, *Synchronization: A Universal Concept in Nonlinear Sciences*, Vol. 12 (Cambridge university press, Cambridge, 2003).
- [26] M. A. Zaks, A. B. Neiman, S. Feistel, and L. Schimansky-Geier, *Phys. Rev. E* **68** (2003).
- [27] D. S. Goldobin, I. V. Tyulkina, L. S. Klimenko, and A. Pikovsky, *Chaos* **28**, 101101 (2018).
- [28] I. V. Tyulkina, D. S. Goldobin, L. S. Klimenko, and A. Pikovsky, *Phys. Rev. Lett.* **120** (2018).
- [29] H. Makare, H. N. Pishkenari, and G. R. Vossoughi, *Nonlinear Dyn.* **89**, 2609 (2017).
- [30] E. Ott and T. M. Antonsen, *Chaos* **19**, 023117 (2009).
- [31] L. M. Childs and S. H. Strogatz, *Chaos* **18**, 043128 (2008).
- [32] In stochastic processes, the closure $\langle x^3 \rangle \simeq \langle x \rangle^3 + 3\langle x \rangle \langle x^2 \rangle$ is also called *Gaussian closure* because it assumes that the variable x follows Gaussian statistics. Note that in the case under study, assuming that Z obeys Gaussian statistics and considering that ψ is Gaussian distributed are two different approximations.
- [33] I. Lima Dias Pinto and M. Copelli, *Phys. Rev. E* **100**, 062416 (2019).
- [34] It is important to distinguish between the interspike interval of each single unit, and the interval between any two consecutive spikes in a network. When looking at avalanches, the second option is preferred, since it gives a small timescale able to resolve the internal structure of avalanches. On the other hand, to measure the CV one focuses on inter-spike intervals of individual oscillators.
- [35] As a side remark, let us emphasize that a perfectly phase-synchronous state does not exist in 2D [24], as it happens in well-known models of equilibrium statistical mechanics [36] and also in the Kuramoto model [13], as rotational symmetry cannot possibly be broken in low-dimensional systems; there are always some “topological defects” in the system preventing it to exhibit perfect synchronization.
- [36] N. D. Mermin and H. Wagner, *Phys. Rev. Lett.* **17**, 1133 (1966).